Atmospheric Research 176–177 (2016) 29–42

Contents lists available at ScienceDirect

Atmospheric Research

journal homepage: www.elsevier.com/locate/atmosres

Examining the influence of meteorological simulations forced by different initial and boundary conditions in volcanic ash dispersion modelling

Gabriela C. Mulena [a,c,*], David G. Allende [a], Salvador E. Puliafito [a,b,c], Susan G. Lakkis [b,d], Pablo G. Cremades [a,c], Ana G. Ulke [e,f]

[a] Grupo de Estudios Atmosféricos y Ambientales, Facultad Regional Mendoza, Universidad Tecnológica Nacional (UTN), Mendoza, Argentina
[b] Facultad Regional Buenos Aires, Universidad Tecnológica Nacional (UTN), Buenos Aires, Argentina
[c] Consejo Nacional de Investigaciones Científicas y Técnicas (CONICET), Av. Rivadavia 1917 (C1033AAJ), Ciudad Autónoma de Buenos Aires, Argentina
[d] Facultad de Ciencias Agrarias, Pontificia Universidad Católica Argentina, Buenos Aires, Argentina
[e] Departamento de Ciencias de la Atmósfera y los Océanos, Facultad de Ciencias Exactas y Naturales, Universidad de Buenos Aires (UBA), Buenos Aires, Argentina
[f] Unidad Mixta Internacional (UMI), Instituto Franco Argentino sobre Estudios de Clima y sus Impactos (IFAECI)/Centre National de la Recherche Scientifique (CNRS), Intendente Güiraldes 2160, Ciudad Universitaria Pabellón II - 2do. piso (C1428EGA), Buenos Aires, Argentina

ARTICLE INFO

Article history:
Received 29 September 2015
Received in revised form 5 February 2016
Accepted 10 February 2016
Available online 20 February 2016

Keywords:
FALL3D
NCEP-GFS analysis
ERA Interim reanalysis
WRF
2011 Puyehue–Cordón Caulle Complex eruption

ABSTRACT

The performance of the combination of the FALL3D ash dispersion model with the Weather Research and Forecast (WRF) meteorological model in the southern cone of South America under two initial and boundary conditions was evaluated. ERA-Interim and NCEP-GFS datasets were used as dynamic conditions by WRF to simulate meteorological fields for FALL3D. As a study case, we used the eruption of the Puyehue–Cordón Caulle Volcanic Complex occurred in Chile in June 2011. The simulated meteorological results were compared with the horizontal wind direction, meridional and zonal wind components, air and dew point temperatures of 7 radio sounding stations using a set of error indicators. In addition, the ash mass load simulated by FALL3D for a day of maximum dispersion of volcanic ash was evaluated using the Moderate Resolution Imaging Spectroradiometer (MODIS) data, on which the Prata algorithm was applied. As well as this, the WRF-dominant physical processes with both dynamic conditions were analyzed for that same date.

Meteorological results indicated that the simulation performed with WRF and NCEP-GFS shows the lowest errors at levels between 925 and 300 hPa. Ash dispersion simulated with FALL3D and WRF in both dynamic conditions shows a different perfomance, which from the synoptic and dynamic viewpoint can be explained for the result of wind intensity and geopotential height. Moreover, WRF intiliazed with NCEP-GFS and FALL3D has a higher degree of concordance with the MODIS image. Based on the analysis and results, it was concluded that for the southern cone of South America, 1) it was not trivial for the simulation of volcanic ash dispersion to use one dynamic condition or another in WRF; 2) in that sense, meteorological variables that influenced the differences in volcanic ash dispersion were horizontal wind intensity and direction and geopotential heights; 3) the system generated from the combination of the WRF model initialized with NCEP-GFS and the FALL3D dispersion model would provide better estimations of ash plume position and deposition in the region.

1. Introduction

Emissions from volcanoes can affect human health (Rojas-Ramos et al., 2001; Spence et al., 2005a), agriculture and livestock (Wilson et al., 2011), settlements and infrastructure (Spence et al., 2005b), and also represent a serious hazard to airplanes and airport operations (Gislason et al., 2011).

Specially, the aircraft encounters with volcanic ash clouds have endangered the lives of tens of thousands of passengers and produced severe economic disruption caused by physical damage of aircraft, diversion and cancellation of flight (Casadevall, 1994; Miller and Casadevall, 2000; Guffanti et al., 2008, 2010). The hazards associated with aircraft-ash interactions are not restricted to zone near volcanoes but also include those in transit over volcanic or even non-volcanic areas (Siebert et al., 2010; Kvietkus et al., 2013). In this sense, in a recent study over Spain, Adame et al. (2015) confirmed the importance to evaluate the impact probability of the ash cloud and the arrival time at a particular location. Casadevall and Krohn (1995) described how the 1992 Crater Peak eruption cloud of Mount Spurr reached as far as the Cleveland Air Traffic Control Center, approximately 5000 km from the volcano, and affected aviation operations in the United States and Canada. Simpson et al. (2002) described a possible aircraft-ash encounter in northern California from the 2001 Mount Cleveland eruptions,

* Corresponding author.
E-mail address: celeste.mulena@frm.utn.edu.ar (G.C. Mulena).

http://dx.doi.org/10.1016/j.atmosres.2016.02.009
0169-8095/

approximately 3000 km from the volcano. These incidents have prompted the establishment of cooperative efforts by the International Civil Aviation Organization (ICAO) and the volcanological community to monitor and forecast ash clouds movement and dispersion so that they can be avoided damage to air navigation.

In this direction, several Volcanic Ash Transport and Dispersion Models (hereinafter VATDMs) are routinely used by Volcanic Ash Advisory Centers (VAACs) designed by ICAO to forecast ash cloud location and issue periodic Volcanic Ash Advisories. Other VATDMs are employed to model ash-fall deposits and concentration especially in urbanized areas near volcanoes (Macedonio et al., 2005; Scollo et al., 2009; Bonasia et al., 2012). For example, the London VAAC's capability to forecast the transport and spread of volcanic ash for flight safety on the Northeast Atlantic routes is delivered by the Numerical Atmospheric-dispersion Modelling Environment (NAME: Ryall and Maryon, 1998). The London VAAC adopts threshold ash concentration values that were employed during the 2010 eruptions of Eyjafjallajökull in Iceland (Witham et al., 2012). According to this, there are zones of low (ash concentration between 200 and 2000 μg/m^3), medium (between 2000 and 4000 μg/m^3) and high (>4000 μg/m^3) contamination. The high contamination area is classified as dangerous and thus airline carriers do not authorize their flights.

The effects of uncertainties in volcanic parameters (i.e. Mass Flow Rate, Total Grain Size Distribution, height and shape of eruption column) in VATDMs have been deeply discussed by Scollo et al. (2008) and references within. However, the importance of the representation of the meteorological fields in VATDMs has been scarcely discussed. For instance, Woodhouse et al. (2013) emphasize that the wind fields must be determined appropriately to prevent significant underestimations of the mass flow of the volcanic source during an eruption. Furthermore, Tsunematsu et al. (2008), stress the importance of local wind circulation to determine the receptors affected by the volcanic ash deposition.

An inappropriate representation of the meteorological fields and the geographical characteristics can lead to errors in the numerical simulations of the transport of chemical species, aerosols, and particulate matter (Hanna and Strimaitis, 1990; Brioude et al., 2012). In particular, many studies reveal that errors in wind direction are the most important because they directly affect the dispersion mechanisms of pollutants (mainly transport and dilution) and make it difficult to properly identify the potentially affected areas. Furthermore, the uncertainty in temperature and wind intensity data affects the calculation of dispersion parameters such as the Monin–Obukhov length, atmospheric stability and friction velocity. Moreover, errors in precipitations could have an influence on the simulation of wet scavenging of soluble gases and aerosol particles (Scott and Luecken, 1992; Andronache, 2004; Spiridonov and Ćurić, 2012). Additionally, an imprecise characterization of the terrain is reflected in uncertainties in surface temperature and in turbulent flows (Sertel et al., 2010; Katurji et al., 2011).

In most cases, meteorological fields used in VATDMs are obtained from mesoscale meteorological models such as the Weather Research and Forecasting Model (WRF: Michalakes et al., 2004), the Fifth-Generation Penn State/NCAR Mesoscale Model (MM5: MM5 Community Model Homepage, n.d.), or directly using global models' data like those provided by the European Centre Medium-Range Weather Forecasting ERA-Interim reanalysis (ERA-Interim: Dee et al., 2011), the National Centers for Environmental Prediction/Global Forecast System analysis (NCEP-GFS: Unidata/University Corporation for Atmospheric Research, UCAR et al., 2003) and the United Kingdom Met Office Unified Model (UK Met Office Unified Model: Cullen, 1993), among others. The advantage of using mesoscale meteorological models lies in the fact that these have better spatial and temporal resolution than global datasets and include detailed static data (i.e., detailed topography, land cover, vegetation, surface heterogeneities, and roughness), which also allows to address meteorological phenomena achieving a better representation of the local regime in addition to the representation of the relevant mesoscale process. In that sense, to optimize mesoscale meteorological models, in a particular area, it is necessary to perform a detailed evaluation of the most appropriate configuration for the model, in particular, regarding dynamic conditions (that is, initial and boundary conditions derived from reanalysis or analysis data) that will be introduced in it (Carvalho et al., 2012). Both, reanalyses and analyses global products have been employed for modelling weather studies over short and long periods of time (Merzlyakov et al., 2013; Carvalho et al., 2014; Kuo et al., 2014). Due to continuous evolution and progress in the development of initial and boundary conditions, ERA-Interim and NCEP-GFS are currently the reanalysis/analysis datasets that are freely and publicly available and continue to be kept up-to-date (Carvalho et al. (2014) and references within). Summarized information about these datasets is shown in Table 1.

To the best of the author's knowledge, there is no literature on regional and long-distance ash transport modeling that compares the influence of boundary and initial dynamic conditions on ash dispersion. Moreover, there are no studies about the propagation of errors of meteorological fields in VATDMs.

In this work, we evaluated the influence of two dynamic conditions, ERA-Interim reanalysis and NCEP-GFS analysis, as input to the WRF model on the simulation of volcanic ash dispersion with the FALL3D model, in the southern cone of South America. As a case of analysis, the recent eruption occurred in June 2011 in the Puyehue–Cordón Caulle Volcanic Complex (PCCVC) located in the Andes Range was studied. The experiments were performed from 3 to 13 June 2011 along 1200 km downwind of the volcanic complex.

We proposed that WRF is sensitive to the change in the dynamic conditions (NCEP-GFS and ERA-Interim) and, therefore, the latter can affect the simulation of volcanic ash dispersion with FALL3D. For that purpose, the uncertainties in horizontal wind direction, zonal and meridional wind components, air and dew point temperatures derived from the WRF model combined with NCEP-GFS and ERA-Interim through the errors detailed in Section 2.2.3 were evaluated. Although we supposed that the major meteorological uncertainty was in the horizontal wind direction, the remaining variables were also evaluated in order to assess this hypothesis. Then, we evaluated the dominant physical processes of the WRF model, combined with the two initial and boundary conditions that contributed to the net transport of the volcanic plume on June 6, 2011, when the ash dispersion was larger and extended in different directions.

2. Materials and methods

2.1. Study case

There are more than 70 active volcanoes located in the Andes Range on the border between Argentina and Chile, belonging to the subduction zone of the Pacific underneath the Andean plate straddling the whole west coast of South America (Siebert and Simkin, 2002). The largest active geothermal area of the Southern Volcanic Zone (SVZ) of the Chilean Andes is PCCVC (Lara et al., 2006). The Complex is located in a portion of the Patagonia region (the southern end of South America between 36°S and 55°S) which has a high topographic complexity (Fig. 1).

The climatological mean fields of surface pressure show that Patagonia is located between the southern region of the semi-permanent subtropical belt of high pressures, whose direct influence extends to approximately 40°S, and the low subpolar pressures in high latitudes. These pressure systems have only small seasonal variations and spatial variabilities dependent on large-scale atmospheric circulation. As a result of this mean configuration of pressures, western winds prevail all year long in Patagonia. Atmospheric circulation, as well as climatological behavior, is affected by transient phenomena of lesser temporal and spatial scales, such as synoptic-scale perturbations. In particular, in the winter of the South Hemisphere, the region is under

Table 1
Main characteristics of the NCEP-GFS and ERA-Interim datasets.

Datasets	Type of dataset	Horizontal resolution	Standard pressure levels	Vertical sigma levels	Temporal resolution	Time coverage	Assimilation system
NCEP-GFS	Analysis	0.5°×0.5° (~55 km horizontal resolution)	26 (from 1000 to 10 hPa)	60	Each 6 hours	2004–present	6-hourly 3D-VAR
ERA-Interim	Reanalysis	0.75°× 0.75° (~79 km horizontal resolution)	37 (1000 to 1 hPa)	64	Each 6 hours	1979–near present	12-hourly 4D-VAR

the influence of cold front passages and post-frontal anticyclonic systems (Satyamurty et al., 1998). These systems generally move from West to East or from Southwest to Northeast. The characteristics and behavior of these systems are determined essentially by the thermal-hydrodynamics of the middle and high levels of the troposphere (Raga et al., 2013).

The most recent PCCVC's eruptive event started on June 4, 2011, at 18:45 UTC with the opening of a new vent (40.52°S, 72.17°W), which was located at a distance of about 7 km north–northwest from the crater rim of the Puyehue volcano. This eruption continued very powerfully for the next 3 days and developed a vigorous sustained eruption column that rose 10–12 km. Westerly winds drifted the plume round the Southern Hemisphere, which reached Australia in a week. Airports as far away as Buenos Aires (34.56°S, 58.41°W) and Melbourne (37.82°S, 144.96°E) had to be temporarily closed due to volcanic ash (Bulletin of the Global Volcanism Network, BGVN, 2012). The event continued being monitored during June and the following months.

2.2. Modelling system

2.2.1. Meteorological simulations

The WRF model is a fully compressible, Eulerian non-hydrostatic meteorological mesoscale model that solves the equations of atmospheric motion (Michalakes et al., 2004; Skamarock et al., 2008). WRF time-dependent meteorological data (wind field, air and dew point temperatures, etc.) and topographic description were ingested into the FALL3D model (see Section 2.2.2) to simulate the spatial and temporal evolution of PCCVC's volcanic ash dispersion. In this work, we employed the version 3.4 of the WRF model to conduct two different simulations with different dynamic initial and boundary conditions:

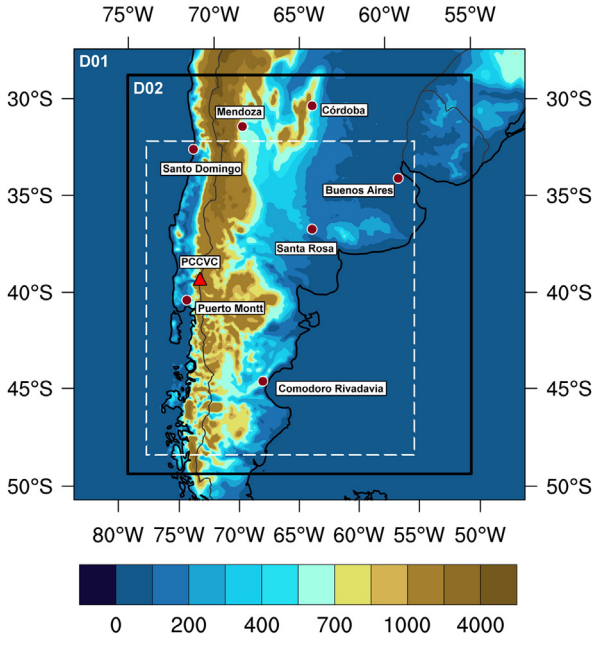

Fig. 1. Modeling domains (D01 and D02) for the WRF model (solid lines) and FALL3D model (dotted line) containing terrain elevations (m.a.s.l.). Red dots indicate the upper air meteorological sites. The triangle indicates the location of the PCCVC.

NCEP-GFS analysis and ERA-Interim reanalysis. We called these simulations WRF_GFS and WRF_ERA, respectively, and in this sense, the meteorological configurations used with the ash dispersion model were referred to as FALL3D + WRF_GFS and FALL3D + WRF_ERA. WRF simulations covered from June 3, 2011, at 00:00 UTC to June 13, 2011, at 00:00 UTC. In order to illustrate the differences already present in the analysis/reanalysis data, the air-temperature fields by NCEP-GFS and ERA-Interim at different standard pressure levels can be observed in Appendix A.

The meteorological simulations were configured with two domains using the two-way nesting strategy (Fig. 1). Due to the fact that the different global datasets considered here have different spatial resolutions, in order to achieve a common size and resolution of the innermost domain, a 3:1 grid ratio between inner and outer nest was well established to be the optimal ratio for nesting WRF domains. The outermost domain was centered at 40.12°S and 64.99°W, had a horizontal resolution of 27 km and covered a total area of approximately 2700×2700 km^2. The innermost domain with 9 km of horizontal resolution was employed by the FALL3D model as meteorological inputs (Section 2.2.2) and used for the meteorological modelling evaluation (Section 2.2.3). The vertical structure of the model was divided into 28 terrain-following hydrostatic pressure levels (Laprise, 1992), with the top level being located at 50 hPa.

All simulations used the same physical options: the Yonsei University Planetary Boundary Layer model (Hong, 2010), the Unified Noah Land Surface model (Ek et al., 2003), the WRF Single-Moment 5-class microphysics scheme (Hong et al., 2004), the Rapid Radiative Transfer Model long-wave Radiation (Mlawer et al., 1997), the Dudhia parameterization for the Short-Wave Radiation (Dudhia, 1989), and the Kain–Fritsch cumulus parameterization (Kain, 2004). The grid nudging option of the WRF's Four-Dimensional Data Assimilation (FDDA) system was used in all simulations, as suggested by Carvalho et al. (2012). However, to avoid possible interferences in the resolved mesoscale forcing mechanisms that are important to the development of the boundary layer (Borge et al., 2008), no nudging was applied inside the Planetary Boundary Layer. A more detailed description of this technique can be found in Skamarock et al. (2008).

The complex topography in the western portion of the modelling domain requires the inclusion of accurate terrain descriptions, since topographic perturbations cause large changes in wind speed and direction and in the turbulent fluxes that strongly affect ash dispersion. Then, the default topographic data in WRF were updated using the Shuttle Radar Topography Mission (SRTM3) data (Rodriguez et al., 2005). Moreover, the standard USGS Land Use/Land Cover (LULC) scheme with a horizontal resolution of 1 km was modified by means of a customized ~280 m resolution dataset (Puliafito et al., 2015).

2.2.2. Ash transport modelling

FALL3D is a three-dimensional time-dependent Eulerian model for the simulation of transport, dispersion and deposition of volcanic ashes and lapilli (Costa et al., 2006; Folch et al., 2009). The model solves the advection–diffusion–sedimentation equation on a structured terrain-following grid using a second-order finite differences explicit scheme. Each particle class is characterized by particle diameter, density, and shape. Numerical simulations of different eruptions using FALL3D have been previously performed to validate the model (for example, Folch et al., 2012; Scaini et al., 2012). The model is capable of simulating the ash concentration at specific Flight Levels (FL) of

relevance for flight operations and the ash mass load, among other variables. A FL is barometric pressure, expressed as a standard nominal altitude in hundreds of feet which represents the vertical distance of an aircraft above the isobaric surface of 1013.25 hPa, namely, pressure at sea level. For example, FL50 is referred to as "flight level 50," equivalent to 5000 ft a.s.l. (~1500 m.a.s.l.) or 850 hPa.

The computational volcanic domain was located between longitude 75.70°W to 57.75°W and latitude 32.8°S to 48.6°S, with an altitude of 16 km at the top (Fig. 1). The spatial discretization contained $100 \times 100 \times 31$ points corresponding to a horizontal grid spacing of ~10 km and a vertical grid spacing of ~500 m. The simulation covered from June 4 at 19:15 UTC (the beginning of the eruption) to June 13 at 00:00 UTC. The meteorological inputs were taken from the WRF innermost domain at 9 km horizontal resolution (see Section 2.2.1), and then they were hourly interpolated to the FALL3D mesh.

In this study, the Mass Flow Rate (MFR) was estimated by means of the eruption column model implemented in FALL3D, based on the Buoyant Plume Theory (BPT: Bursik, 2001; Carazzo et al., 2006). This eruption column model allowed the computation of MFR and the vertical distribution of mass, which are a function of column height and mixture properties at the vent (exit temperature, velocity, water content, and Total Grain Size Distribution (TGSD)). In that sense, we input the model column height calculations consistent with observations made by the Chile's National Service of Geology and Mining (SERNAGEOMIN, 2011). In addition, conditions at the vent were set to an exit velocity of 200 m/s, a water content of 3% (by weight) in the magma, and an exit temperature of 1150 °C, values compatible with a Subplinian-type eruption (Sulpizio et al., 2005). MFR was obtained using the BPT model and ranged between 6×10^{-5} kg/s and 8×10^{5} kg/s during the simulated period. The estimated erupted mass was approximately 0.6×10^{11} kg, 85% of which was deposited.

The TGSD depends on the eruption style and intensity and may vary from one eruption phase to another. For modelling purposes, we assumed a TGSD grouped in 7 particle classes with diameters: 4 mm, 1.26 mm, 0.4 mm, 0.13 mm, 0.04 mm, 12.4 μm, and 4 μm. Since data available for shapes of volcanic particles are relatively scarce, we set particle sphericity to 0.90 for all particle classes. TGSD was assumed to be Bi-Gaussian grain-size with mean diameters and dispersion values of 500–700 μm and 125–500 μm, respectively. For fine particles settling velocity estimation, we chose the Ganser (1993) model; for the horizontal diffusion, we used the Community Multiscale Air Quality (CMAQ) model (Byun and Schere, 2006); and we calculated the vertical diffusion term with Similarity option (Costa et al., 2006).

2.2.3. Meteorological modelling evaluation

Observed horizontal wind direction (WD), zonal and meridional wind components (U and V), and air and dew point temperatures (Ta and Td) at mandatory levels from 7 upper-air stations located at different topographic conditions from Argentina and Chile were compared with the WRF simulations (WRF_GFS and WRF_ERA) derived by the innermost domain of 9 km grid spacing (Fig. 1). We must emphasize that the radio soundings available for our study come from stations located north of latitude 40°S and are sparse and discontinuous on time. The density of atmospheric rawinsonde observations employed in the Three-Dimensional Variational with a 6-hour analysis window (6-hourly 3D-VAR) and Four-Dimensional Variational with a 12-hour analysis window (12-hourly 4D-VAR) Data Assimilation systems for NCEP-GFS and ERA-Interim, respectively, for the study period is depicted in Table 2. NCEP-GFS employed the majority of the weather stations mentioned in Table 2 at 12:00 UTC, but at 00 UTC, only stations located at Easter Island and Santo Domingo were used. However, the ERA-Interim documentation only indicates the list of radiosonde stations covering the period from ~1970 to December 2011. Any other particular information about specific observation type (time, day, and station) is not publicly available. This situation is expressed in ERA-Interim column in Table 2 with blank cells.

Agreement between simulated and measured values for all variables at mandatory levels was evaluated using several performance parameters: root mean square error or total error (RMSE), mean bias error (MBE), unbiased root mean square difference (RMSD), variability error (σbias), dispersion or phase error (DISP), and amplitude error (MBE + σbias). A detailed description of selected values and their relation with the model performance can be found in Appendix B. Moreover, the same statistical parameters were used to analyze the simulated horizontal wind directions. Since this is a variable vector, we used the mathematical expressions proposed and described in Berens (2009) and Carvalho et al. (2012).

As an example, Table 3 shows the performance evaluation of both configurations for WD for the 1000 hPa level, in each upper-air station and for the different types of error. In Table 3, it can be observed that in each station, the configuration with the best behavior or success was chosen; namely, that which generated the minimum error in absolute value. Here, for instance, we see that in the Santo Domingo station (Chile), the minimum MBE and σbias were given by WRF_ERA. However, in the same city, the minimums of DISP, RMSD and RMSE were given by WRF_GFS. The MBE + σbias sum constitutes the amplitude error, which in WD at 1000 hPa was equally represented by both

Table 2
Summarized information about upper-air station used by NCEP-GFS, ERA-Interim and our study.

Country	ID WMO[a]	Latitude (°S)	Longitude (°W)	Altitude (m.a.s.l.)	Upper-air station	NCEP-GFS	ERA-Interim[b]	This study[c]
Chile	85442	23.43	70.43	120	Antofagasta/Cerro	*		
	85469	27.15	109.42	47	Easter Island	*		
	85543	32.78	71.52	8	Quintero (Mil)			
	85574	33.38	70.78	476	Pudahuel/Arturo			
	85586	33.65	71.62	75	Santo Domingo	*		*
	85799	41.42	73.08	86	Puerto Montt/Tepual	*		*
	85934	53.00	70.85	37	Punta Arena	*		
Argentina	87047	24.85	65.48	1216	Salta	*		
	87155	27.45	59.05	52	Resistencia	*		
	87344	31.32	64.22	474	Córdoba	*		*
	87418	32.83	68.78	704	Mendoza/El Plumerillo	*		*
	87576	34.82	58.53	20	Buenos Aires/Ezeiza	*		*
	87623	36.57	64.27	191	Santa Rosa	*		*
	87715	38.95	68.13	271	Neuquén			
	87860	45.78	67.50	46	Comodoro Rivadavia	*		*

[a] ID WMO is a five-digit number (ID) assigned to this weather station by the World Meteorological Organization (WMO): ftp://ftp.wmo.int/wmo-ddbs/Radiosondes.xls.
[b] The blank cells indicate that information about specific observation type (time, day, and station) is not publicly available.
[c] Upper-air stations located within the innermost domain of 9 km grid spacing (D02) in Fig. 1.

Table 3
Relative frequency for the full set of statistical indicators and upper air stations for wind direction (WD) at 1000 hPa.

Errors					
Upper-air stations	RMSE	MBE	obias	DISP	RMSD
Buenos Aires	WRF_GFS	WRF_GFS	WRF_GFS	WRF_GFS	WRF_GFS
Comodoro Rivadavia	—	— (*)	—	—	—
Córdoba	—	—	—	—	—
Mendoza	—	—	—	—	—
Puerto Montt	WRF_GFS	WRF_GFS	WRF_ERA	WRF_GFS	WRF_GFS
Santa Rosa	—	—	—	—	—
Santo Domingo	WRF_GFS	WRF_ERA	WRF_ERA	WRF_GFS	WRF_GFS
Total WRF_GFS	3	2	1	3	3
Total WRF_ERA	0	1	2	0	0
Relative frequency of WRF_GFS	4.1	2.7	1.4	4.4	4.1
Relative frequency of WRF_ERA	0.0	1.4	2.7	0.0	0.0
N	73	73	73	68	73

(*) The mark (-) indicates that both configurations have the same results.

configurations. Finally, the relative frequency of each configuration was defined. For that, we counted the total number of cases for each model configuration that represented the best scenario and we scaled them with total sample size (N). N is given by the sum of the sub-sample sizes in each type of error, i.e., the number of cases counted as success for WRF_GFS + the number of cases counted as success for WRF_ERA, for all mandatory levels. The sample size will depend on the number of mandatory levels with valid data and the number of best agreement coincidences. In Tables 4 and 5, the relative cumulative frequency of WRF_GFS and WRF_ERA is the sum of all the relative frequencies at all mandatory levels and for each configuration. It is important to note that the statistical parameters that equalized (due to the absence of observational data, for instance) were not considered.

2.2.4. Volcanic modeling evaluation

Space-borne remote sensing has long been a key tool in volcanic ash detection and monitoring (e.g., Shibata and Kinoshita, 2016). Meteorological and volcanic ash cloud discrimination using remote sensing is based on average properties of volcanic aerosols (Prata, 1989; Yu et al., 2002). Prata (1989) found that the Brightness Temperature Difference (BTD) at 10.8 and 11.9 μm is negative for a volcanic cloud and positive for a meteorological cloud, due to the stronger dispersive nature of silicates compared to water and ice particles.

MODIS, on-board the Terra (EOS AM) and Aqua (EOS PM) satellites, is a passive, imaging spectroradiometer carrying 490 detectors, arranged in 36 spectral bands that cover the visible and infrared spectrum (King et al., 1992). Both satellites are polar-orbiting, with Terra on a descending orbit (southward) over the equator about 10:30 local sun time, and Aqua on an ascending orbit (northward) over the equator about 13:30 local sun time (Guenther et al., 1998). MODIS offers a daily coverage of the Earth, a very important attribute to study volcanic processes which are sporadic and dynamic events. Due to its spectral characteristics, MODIS data can be used to quantify volcanic ash, ice, sulphates, and sulphur dioxide using their thermal infrared (8–12 μm) transmission signature in high spatial and temporal resolutions.

In this work, the MODIS Level-1B calibrated and geolocated radiances (MOD02) from Terra products with channels centered on 11 and 12 μm (channel 31 and 32, respectively) was used to identify volcanic ash features based on BTD for June 6, 2011, at 14:25 UTC (Carn et al., 2009; Thomas and Prata, 2011). MOD02 has a high spatio-temporal

Table 4
Relative frequency for all statistical indicators and upper air stations for WD, U, V, Ta y Td: a) RMSE, b) MBE, and c) RMSD.

Variable	Configuration	Mandatory pressure levels (hPa)											N	Relative cumulative frequency (%)
		1000	925	850	700	500	400	300	250	200	150	100		
a) RMSE														
WD [°]	WRF_GFS	4.1	6.8	8.2	6.8	8.2	8.2	6.8	4.1	4.1	6.8	4.1	73	68.5
	WRF_ERA	0.0	2.7	1.4	2.7	1.4	1.4	2.7	5.5	5.5	2.7	5.5		31.5
U [m/s]	WRF_GFS	4.1	5.4	5.4	6.8	6.8	6.8	6.8	5.4	0.0	2.7	5.4	74	55.4
	WRF_ERA	1.4	4.1	4.1	2.7	2.7	2.7	2.7	4.1	9.5	6.8	4.1		44.6
V [m/s]	WRF_GFS	1.4	5.4	6.8	5.4	6.8	6.8	4.1	4.1	1.4	5.4	2.7	74	50.0
	WRF_ERA	4.1	4.1	2.7	4.1	2.7	2.7	5.4	5.4	8.1	4.1	6.8		50.0
Ta [°C]	WRF_GFS	2.7	9.5	8.1	5.4	8.1	6.8	8.1	2.7	4.1	4.1	5.4	74	64.9
	WRF_ERA	2.7	0.0	1.4	4.1	1.4	2.7	1.4	6.8	5.4	5.4	4.1		35.1
Td [°C]	WRF_GFS	0.0	4.4	4.4	5.9	8.8	8.8	7.4	0.0	1.5	0.0	0.0	68	41.2
	WRF_ERA	5.9	5.9	5.9	4.4	1.5	1.5	2.9	8.8	7.4	8.8	5.9		58.8
b) MBE														
WD [°]	WRF_GFS	2.7	5.5	6.8	6.8	6.8	5.5	5.5	4.1	4.1	5.5	4.1	73	57.5
	WRF_ERA	1.4	4.1	2.7	2.7	2.7	4.1	4.1	5.5	5.5	4.1	5.5		42.5
U [m/s]	WRF_GFS	2.7	8.1	8.1	5.4	2.7	4.1	5.4	6.8	1.4	5.4	5.4	74	55.4
	WRF_ERA	2.7	1.4	1.4	4.1	6.8	5.4	4.1	2.7	8.1	4.1	4.1		44.6
V [m/s]	WRF_GFS	4.1	5.4	4.1	2.7	4.1	5.4	5.4	5.4	6.8	2.7	6.8	74	52.7
	WRF_ERA	1.4	4.1	5.4	6.8	5.4	4.1	4.1	4.1	2.7	6.8	2.7		47.3
Ta [°C]	WRF_GFS	0.0	8.1	5.4	6.8	6.8	6.8	2.7	0.0	2.7	1.4	5.4	74	45.9
	WRF_ERA	5.4	1.4	4.1	2.7	2.7	2.7	6.8	9.5	6.8	8.1	4.1		54.1
Td [°C]	WRF_GFS	1.5	7.4	7.4	8.8	7.4	5.9	4.4	0.0	1.5	0.0	0.0	68	44.1
	WRF_ERA	4.4	2.9	2.9	1.5	2.9	4.4	5.9	8.8	7.4	8.8	5.9		55.9
c) RMSD														
WD [°]	WRF_GFS	4.1	5.5	5.5	4.1	4.1	8.2	4.1	4.1	1.4	6.8	1.4	73	49.3
	WRF_ERA	0.0	4.1	4.1	5.5	5.5	1.4	5.5	5.5	8.2	2.7	8.2		50.7
U [m/s]	WRF_GFS	4.1	5.4	5.4	6.8	6.8	6.8	5.4	5.4	4.1	4.1	5.4	74	59.5
	WRF_ERA	1.4	4.1	4.1	2.7	2.7	2.7	4.1	4.1	5.4	5.4	4.1		40.5
V [m/s]	WRF_GFS	1.4	5.4	5.4	4.1	5.4	6.8	2.7	2.7	1.4	5.4	2.7	74	43.2
	WRF_ERA	4.1	4.1	4.1	5.4	4.1	2.7	6.8	6.8	8.1	4.1	6.8		56.8
Ta [°C]	WRF_GFS	4.1	8.1	8.1	5.4	5.4	5.4	9.5	5.4	6.8	5.4	4.1	74	67.6
	WRF_ERA	1.4	1.4	1.4	4.1	4.1	4.1	0.0	4.1	2.7	4.1	5.4		32.4
Td [°C]	WRF_GFS	0.0	2.9	4.4	4.4	8.8	8.8	7.4	0.0	1.5	1.5	2.9	68	42.6
	WRF_ERA	5.9	7.4	5.9	5.9	1.5	1.5	2.9	8.8	7.4	7.4	2.9		57.4

Table 5
Relative frequency for all statistical indicators and upper air stations for WD, U, V, Ta y Td: a) σbias and b) DISP.

Variable	Configuration	Mandatory pressure levels (hPa)											N	Relative cumulative frequency (%)
		1000	925	850	700	500	400	300	250	200	150	100		
a) σbias														
WD [°]	WRF_GFS	1.4	6.8	6.8	6.8	5.5	6.8	6.8	1.4	5.5	5.5	5.5	73	58.9
	WRF_ERA	2.7	2.7	2.7	2.7	4.1	2.7	2.7	8.2	4.1	4.1	4.1		41.1
U [m/s]	WRF_GFS	2.7	5.4	4.1	5.4	5.4	8.1	6.8	6.8	6.8	5.4	5.4	74	62.2
	WRF_ERA	2.7	4.1	5.4	4.1	4.1	1.4	2.7	2.7	2.7	4.1	4.1		37.8
V [m/s]	WRF_GFS	1.4	5.4	4.1	5.4	5.4	1.4	4.1	2.7	4.1	2.7	5.4	74	41.9
	WRF_ERA	4.1	4.1	5.4	4.1	4.1	8.1	5.4	6.8	5.4	6.8	4.1		58.1
Ta [°C]	WRF_GFS	4.1	6.8	5.4	4.1	6.8	6.8	6.8	4.1	5.4	4.1	2.7	74	56.8
	WRF_ERA	1.4	2.7	4.1	5.4	2.7	2.7	2.7	5.4	4.1	5.4	6.8		43.2
Td [°C]	WRF_GFS	1.5	2.9	2.9	4.4	5.9	4.4	4.4	1.5	1.5	8.8	5.9	68	44.1
	WRF_ERA	4.4	7.4	7.4	5.9	4.4	5.9	5.9	7.4	7.4	0.0	0.0		55.9
b) DISP														
WD [°]	WRF_GFS	4.4	5.9	5.9	4.4	4.4	7.4	4.4	2.9	1.5	7.4	1.5	68	50.0
	WRF_ERA	0.0	4.4	4.4	5.9	5.9	1.5	4.4	5.9	7.4	1.5	8.8		50.0
U [m/s]	WRF_GFS	2.9	5.8	4.3	5.8	5.8	5.8	4.3	4.3	2.9	4.3	2.9	69	49.3
	WRF_ERA	2.9	4.3	5.8	4.3	4.3	4.3	4.3	4.3	5.8	4.3	5.8		50.7
V [m/s]	WRF_GFS	2.9	5.8	5.8	4.3	7.2	8.7	4.3	1.4	1.4	4.3	1.4	69	47.8
	WRF_ERA	2.9	4.3	4.3	5.8	2.9	1.4	4.3	7.2	7.2	4.3	7.2		52.2
Ta [°C]	WRF_GFS	4.3	7.1	7.1	4.3	4.3	5.7	8.6	7.1	5.7	4.3	4.3	70	62.9
	WRF_ERA	1.4	2.9	2.9	5.7	5.7	4.3	1.4	1.4	2.9	4.3	4.3		37.1
Td [°C]	WRF_GFS	0.0	4.7	4.7	6.3	7.8	9.4	7.8	1.6	1.6	0.0	0.0	64	43.7
	WRF_ERA	6.3	6.3	6.3	4.7	3.1	1.6	3.1	6.3	6.3	7.8	4.7		56.3

frequency (1 km pixel resolution, twice per day) and is georeferenced by MODIS geolocation dataset (MOD03) from the same satellite. On the same day, this result was compared with the differences between the ash mass load of FALL3D + WRF_GFS and FALL3D + WRF_ERA. It is well known that the two-band infrared algorithm works best when the eruption is large and strong (Rose and Mayberry, 2000) and where the BTD is large enough to counteract the effects of atmospheric moisture, i.e., in non-tropical ocean regions, as seen in Yu et al. (2002). Moreover, specific environmental conditions like the presence of a cold background scene or the existence of great amounts of water, ice, and large particles ejected in the volcanic cloud can work against the effective use of this technique (Prata et al., 2001). For this reason, in the following section, a BTD (11–12 μm) < −2 K was used to facilitate the identification of ash pixels. Moreover, the differences in the ash concentration for several FL provided by FALL3D + WRF_GFS and FALL3D + WRF_ERA and the synoptic and dynamic situation derived from WRF_GFS and WRF_ERA were described for this specific date. Additionally, the differences between the ash mass load of FALL3D + WRF_GFS and FALL3D + WRF_ERA were evaluated for another day.

3. Results

3.1. Sensitivity analysis of the meteorological parameters

Tables 4 and 5 show the behavior of each configuration for all the errors detailed in Section 2.2.3. Table 4a shows the behavior of each configuration in relation to the RMSE total error. According to this table, WD was, in general, more accurately represented by WRF_GFS at pressure levels between 1000 and 300 hPa, while the remaining pressure levels were better evaluated by WRF_ERA. Variables U, V, and Ta have a similar behavior to WD. Comparisons of the two WRF configurations for U and V with observations showed that wind intensity was better represented by WRF_GFS at pressure levels between 925 and 300 hPa. In turn, Td was better represented by WRF_ERA at most levels, except for levels between 700 and 300 hPa. Results for U and V reflect a direct impact on wind intensity and direction.

The contributions of other errors to the RMSE are shown in Tables 4b–c and 5a–b. The accuracy of the configurations was evaluated by means of the MBE (Table 4b) while their precision was evaluated using the RSMD (Table 4c). In addition, the contributions made to the RMSD were evaluated through the σbias (Table 5a) and the DISP (Table 5b). The different types of errors for each variable had tendencies similar to the RMSE.

Although the RMSE cannot be considered as the sum of the amplitude and phase errors or the sum of the accuracy and precision errors, since successful cases were being considered, general behaviors may anyway be described. From Tables 4b–c and 5a–b, we can thus conclude that the best WRF_GFS performance in relation to the RMSE, in general for levels 1000 and 300 hPa, for WD, U, and Ta, was explained by MBE + σbias. However, the WRF_GFS RMSE of the V and Td variables for those same levels was given by DISP. In addition, the best WRF_ERA performance in RMSE, in general observed at high levels, for Ta and Td, was given by MBE + σbias and for WD, U, and V, by DISP.

3.2. Volcanic ash simulation

With PCCVC located at the center left of the image, Fig. 2 shows the dispersion of the volcanic plume along different axes for June 6, 2011, around 14:25 UTC. As it can be observed, the ash plume developed in the northeast direction, then turned southeast and finally moved over the Atlantic Ocean. This typical triangular shape, due to the contribution of ash emissions from earlier hours and to wind configuration, was evidenced by the ash mass load given by FALL3D + WRF_GFS and FALL3D + WRF_ERA, shown in Fig. 2a–b, respectively, and was also captured by the MODIS image, processed by the Prata algorithm (Fig. 2c). Fig. 2d shows the change in direction between the FALL3D + WRF_GFS and the FALL3D + WRF_ERA configurations, mainly observed in the region that stretches between latitudes 37°S and 42°S and longitudes 72°W and 68°W. The area with positive values in Fig. 2d shows the region for which the ash mass load given by FALL3D + WRF_GFS overestimated FALL3D + WRF_ERA (negative values, the opposite condition). The same figure indicates that near the source, the horizontal wind direction given by FALL3D + WRF_GFS developed more toward the North than FALL3D + WRF_ERA, more in accordance with the direction of the plume described by the MODIS image (Fig. 2c) in the northeastern end corresponding to coordinates 37°S–68°W. In this sense, the non-parametric Mann–Whitney *U* test (Mann and Whitney, 1947), with a confidence interval of 95%, applied in the domain stretching between longitudes 75.70°W and 57.75°W and latitudes 32.8°S and 40°S,

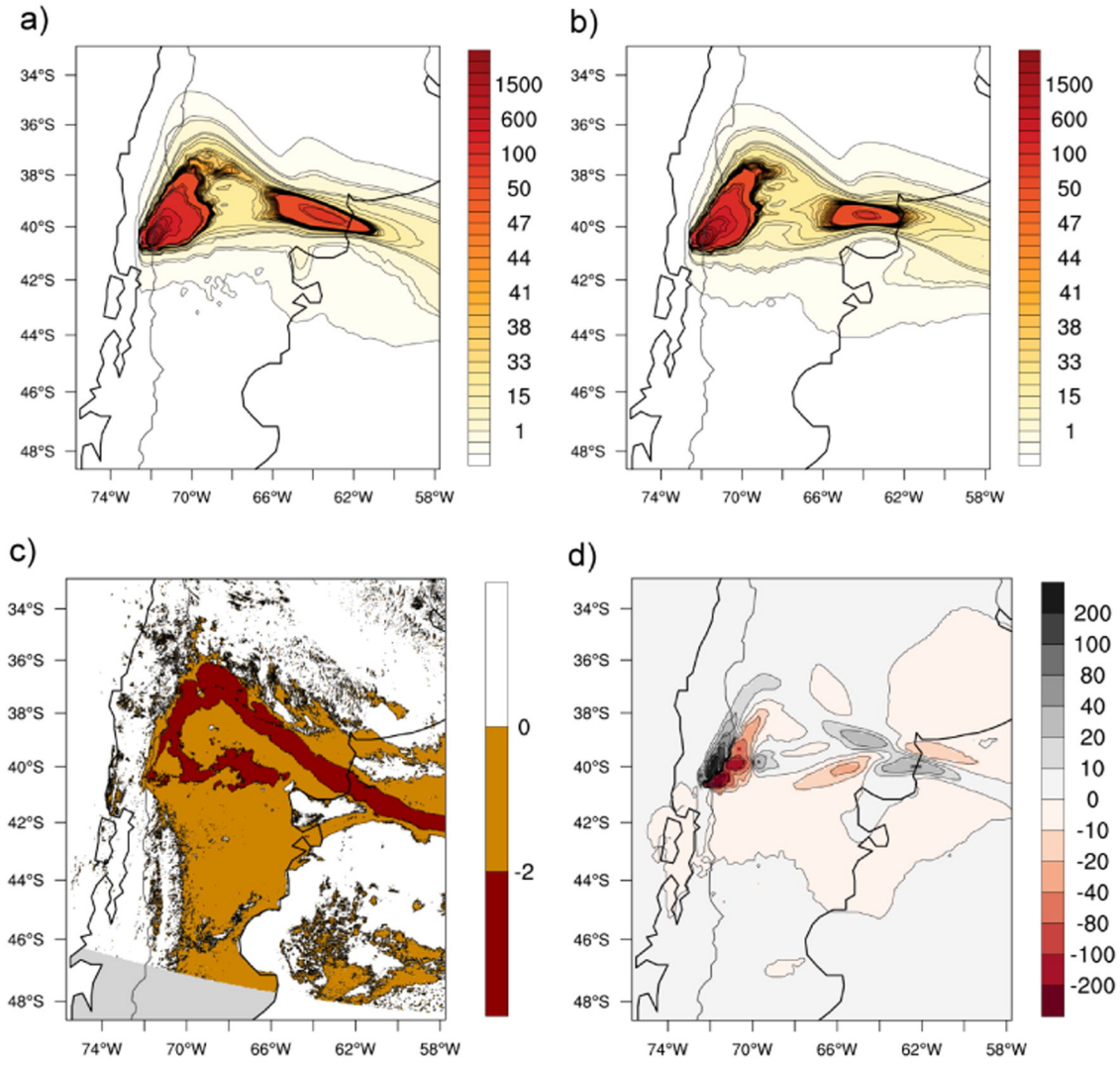

Fig. 2. Ash dispersion for June 6, 2011, at ~14:25 UTC (outputs from FALL3D are averaged for 14:00 UTC and 15:00 UTC): a) Simulated ash mass load (g/m^2) using FALL3D with WRF_GFS configuration; b) simulated ash mass load (g/m^2) using FALL3D with WRF_ERA configuration; c) brightness temperature difference (K), MOD02 Level 1B dataset, d) ash mass load difference (g/m^2) between the simulations FALL3D + WRF_GFS and FALL3D + WRF_ERA (Panel a–Panel b).

indicated that for the ash mass load samples of June 6, 2011, derived from FALL3D + WRF_GFS and FALL3D + WRF_ERA are statistically different ($p < 0.05$).

Fig. 3 shows the differences in the contribution of ash for each height level provided by simulations FALL3D + WRF_GFS and FALL3D + WRF_ERA for June 6 at ~14:25 UTC. This figure shows that the mismatch between the two configurations can be observed at the different height levels. However, the non-parametric Mann–Whitney *U* test indicated the concentration levels derived from FALL3D + WRF_GFS and FALL3D + WRF_ERA are statistically different for the levels between 1500 and 5000 m.a.s.l., which correspond to pressure levels between 850 and 500 hPa. As shown in Tables 4 and 5, for WD at these pressure levels, the WRF_GFS RMSE was lower and it mainly consisted of MBE + σbias.

Figs. 4–6 summarize the synoptic and dynamic situation on June 6 at 14:00 UTC at 850, 500, and 300 hPa. Fig. 4 shows the wind speed differences between WRF_GFS and WRF_ERA at these levels. Here, we can see in latitudes above 40°S, that ash spreads more quickly out of the volcanic source due to the wind speed derived from the WRF_GFS configuration. For example, at 850 hPa, the difference in wind speed between the two configurations was of approximately 20%. In Fig. 4, it can be observed that the speeds from WRF_ERA (blue colors) were responsible for erroneously carrying the plume Northeast (Fig. 2d). Fig. 5 shows the geopotential height differences between WRF_GFS and WRF_ERA at 850, 500, and 300 hPa. Geopotential heights of the different constant pressure levels depend on the average temperature of the layer from the surface up to the level under analysis. In this way, the negative geopotential height anomalies (brown colors) in Fig. 5 show that WRF_GFS generates a layer mean temperature that is lower (colder) than the temperature provided by WRF_ERA and, because of this, the thickness of the atmospheric layer is thinner than that shown by WRF_ERA. Fig. 6 shows the vertical velocity anomalies between WRF_GFS and WRF_ERA at 850, 500, and 300 hPa. This figure shows that the largest anomalies in vertical velocity are found north of latitude 40°S and east of the Andes Mountain Range. The negative vertical velocity anomalies (air descending) are related to the cold air masses shown by WRF_GFS in Fig. 5.

Fig. 7 shows the evolution of differences between the ash mass load of FALL3D + WRF_GFS and FALL3D + WRF_ERA. On June 5 at 9:00 UTC, the ash cloud presented a southeast direction, and on June 6 at 2:00 UTC, the ash plume reached an east direction in response to the prevalent winds. On the next day at 1:00 UTC, the ash cloud extended several kilometers in northerly directions and then, at 19:00 UTC, a 1200 km long plume reached again the southern Patagonia in Argentina and the Atlantic Ocean. Fig. 7 also evidences differences in direction between the FALL3D + WRF_GFS and the FALL3D + WRF_ERA configurations

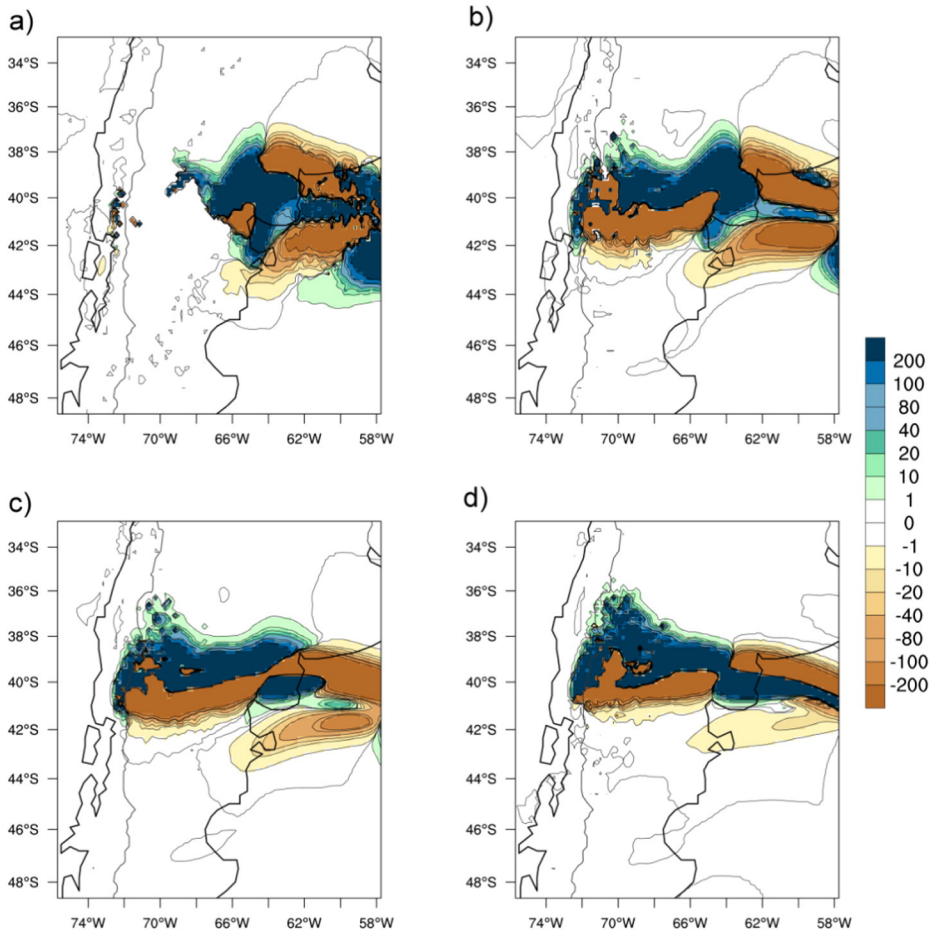

Fig. 3. Concentration difference (μg/m^3) by four levels between the simulations WRF_GFS and WRF_ERA for June 6, 2011, at ~14:25 UTC (outputs from FALL3D are averaged for 14:00 UTC and 15:00 UTC) at: a) 500 m.a.s.l. (~FL20 or 925 hPa); b) 1500 m.a.s.l. (~FL50 or 850 hPa); c) 3000 m.a.s.l. (~FL90 or 700 hPa) and d) 5000 m.a.s.l. (~FL200 or ~500 hPa).

mainly around 40°S. Such as in Fig. 2d, the positive values in Fig. 7 indicate the area where the ash mass load given by FALL3D + WRF_GFS overestimated FALL3D + WRF_ERA (negative values, the opposite condition). In this regard, in the first three stages in the evolution of volcanic ash clouds, when there was great volcanic activity, the Mann–Whitney *U* test revealed significant statistical differences ($p < 0.05$) between simulations. However, on June 7 at 19:00 UTC, ash concentration decreased as a result of lower volcanic activity and, therefore, the statistical difference between the two configurations was not significant. Nevertheless, the differences in ash concentration between the two configurations might be relevant from the receptor's viewpoint.

4. Discussion

Wind direction primarily depends on the spatial distribution and the evolution of the isobaric centers whereas wind speed depends on the intensity of the horizontal pressure gradient.

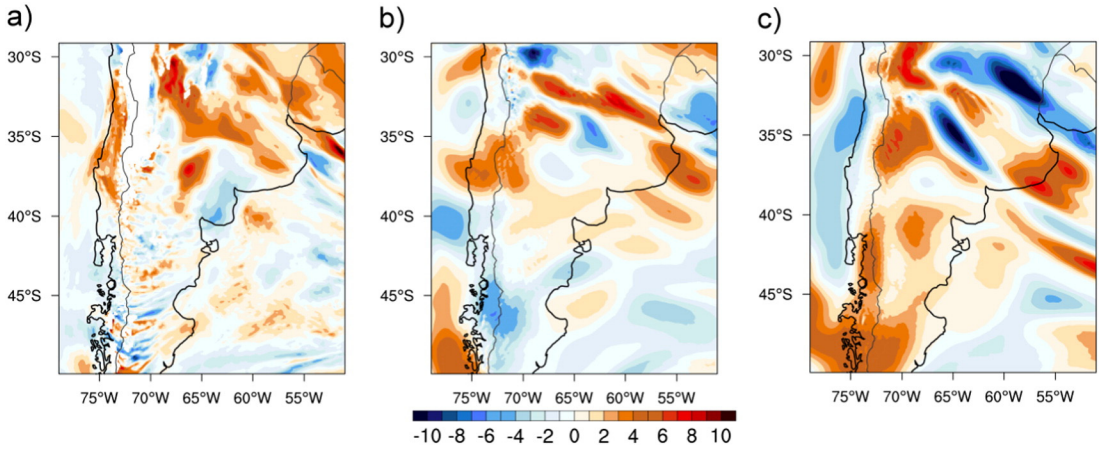

Fig. 4. Horizontal wind speed anomalies (WRF_GFS –WRF_ERA) for June 6, 2011 at 14:00 UTC in m/s at: a) 850 hPa (~FL50 or ~1500 m.a.s.l.); b) 500 hPa (~FL200 or ~5000 m.a.s.l.) and c) 300 hPa (~FL300 or ~9000 m.a.s.l.)

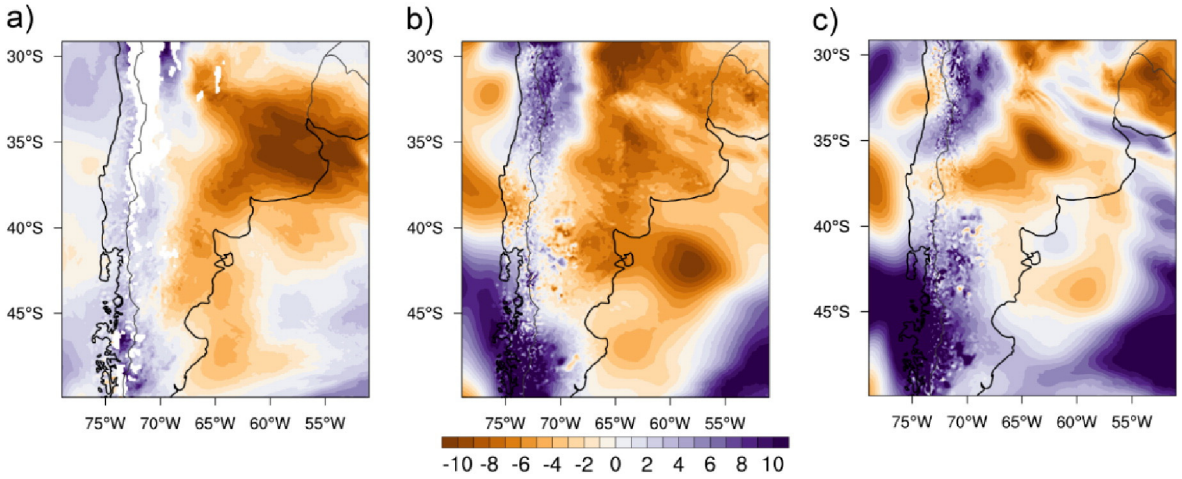

Fig. 5. Geopotential height anomalies (WRF_GFS–WRF_ERA) for June 6, 2011, at 14:00 UTC in gpm at: a) 850 hPa (~FL50 or ~1500 m.a.s.l.); b) 500 hPa (~FL200 or ~5000 m.a.s.l.) and c) 300 hPa (~FL300 or ~9000 m.a.s.l.).

In this work, we have found that changes in horizontal wind direction in the meteorological models resulted in different performances of the dispersion model. According to the analysis of Fig. 2-d, for example, the plume direction described by FALL3D + WRF_GFS (with a higher degree of agreement with the MODIS image) was mismatched by 1° (about 100 km) near the source (and up to 1.5° (about 150 km) at 1000 km from the source), counter-clockwise of the plume direction described by FALL3D + WRF_ERA. This situation can be interpreted as a WD deviation of WRF_GFS toward the West in relation to the WD of WRF_ERA. Even more, the turning of the wind vector with height varies between both configurations due to differences in the simulation of the horizontal temperature advection. A detailed analysis of wind direction during the event showed that only those winds coming from levels of low and intermediate heights (pressures > 300 hPa) are primarily responsible for the net transport of the PCCVC plume at this more intense stage. In addition, a misrepresentation of surface winds due to the complex topography and friction may result in a negative bias in directional transport (delay) of the volcanic plume.

In addition in Fig. 4, differences in wind speeds between WRF_GFS and WRF_ERA (mainly in the pressure levels of 850, 500, and 300 hPa) are also observed due to variations in the geopotential height fields (Fig. 5). This causes the WRF_ERA configuration to predict a more eastward position of the low-pressure systems (advanced system in relation to WRF_GFS). In spite of this, according to Table 5b, WRF_ERA had fewer cases of minimum phase errors for Ta at low and intermediate levels (except for 700 and 500 hPa).

According to this analysis, special attention should be given not only to horizontal wind direction but also to horizontal wind intensity and geopotential heights.

Jet aircraft encounters with volcanic ash between 1980 and 1998 have caused more than 250 million dollars in damage to aircraft engines, avionics, and airframes not only in areas close to the volcanic eruption but also at distances of up to 3000 km from the source (Miller and Casadevall, 2000). In addition, between 1953 and 2009, at least 100 encounters between ash clouds and civil jet aircraft were reported (Fig. 1 in Guffanti et al. (2010)), which is mainly the result of inexistent or inaccurate estimations of ash cloud location. On that subject, during June 2011, the PCCVC eruption caused flight cancellations in Argentina's two main airports located in Buenos Aires: Jorge Newbery and Ezeiza. For example, on 8 June 2011, the simulated

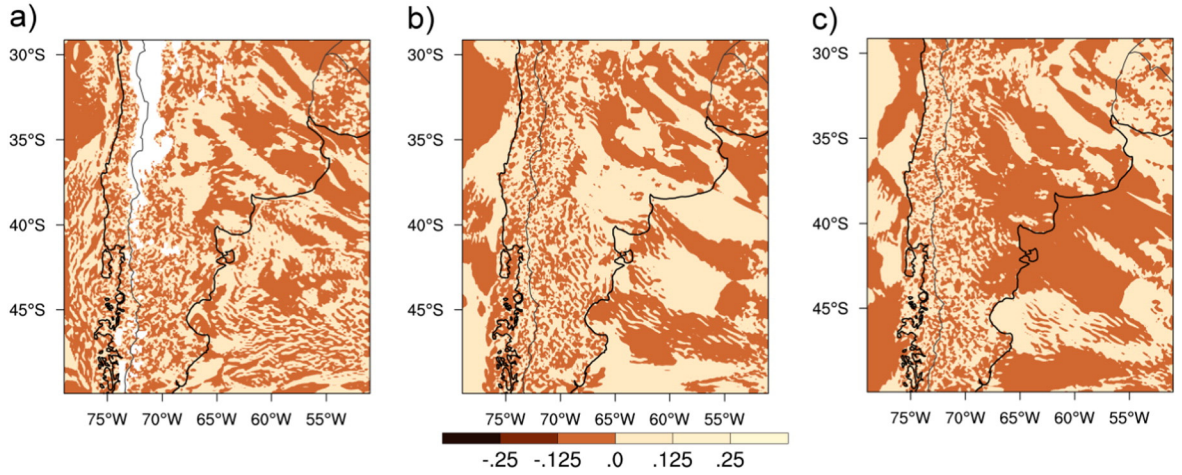

Fig. 6. Vertical velocity anomalies (WRF_GFS–WRF_ERA) for June 6, 2011, at 14:00 UTC in m/s at: a) 850 hPa (~FL50 or ~1500 m.a.s.l.); b) 500 hPa (~FL200 or ~5000 m.a.s.l.) and c) 300 hPa (~FL300 or ~9000 m.a.s.l.).

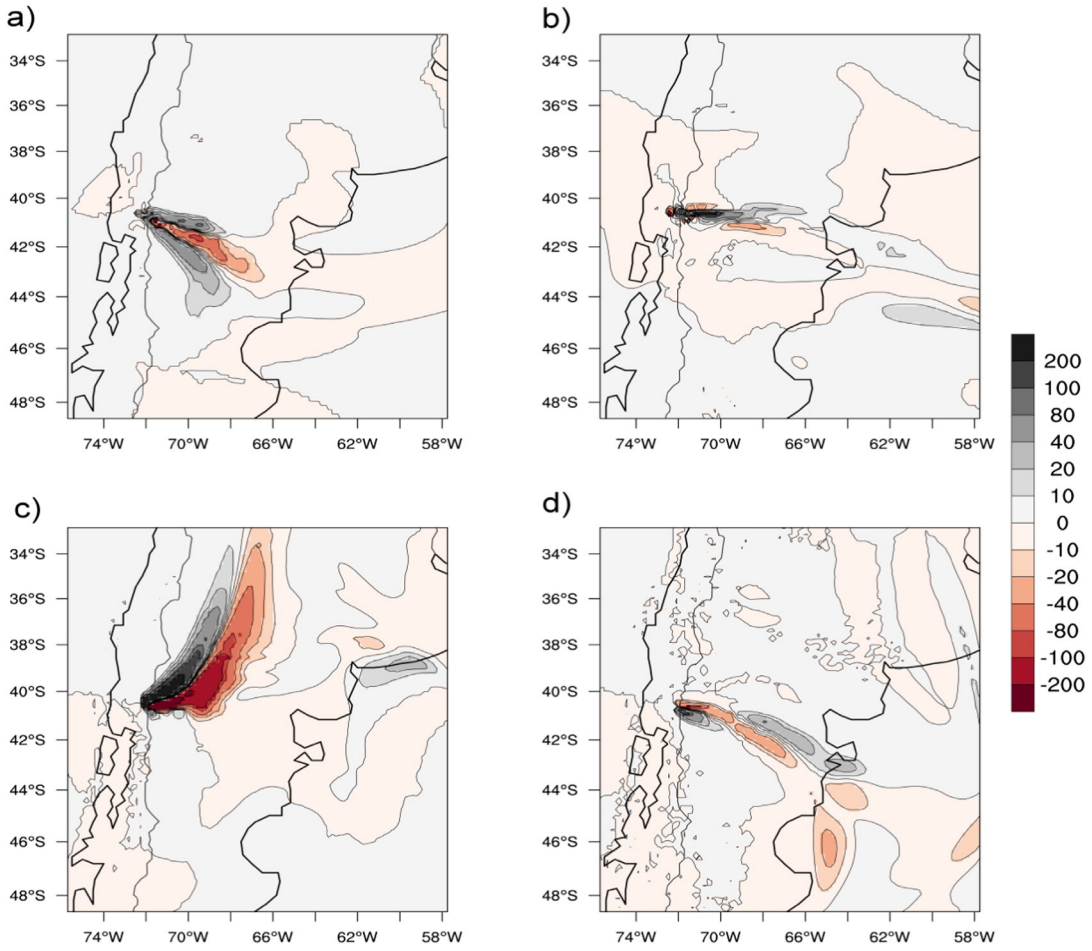

Fig. 7. Ash mass load difference between the simulations FALL3D + WRF_GFS and FALL3D + WRF_ERA in g/m^2 for: a) June 5, 2011, at 9:00 UTC; b) June 6, 2011, at 2:00 UTC; c) June 7, 2011, at 1:00 UTC; d) June 7, 2011, at 19:00 UTC.

concentration at flight levels FL150 and FL300 (which correspond to 5000 and 9000 m.a.s.l., respectively) in both airports were estimated by FALL3D + WRF_GFS to be ~2400 μg/m^3 and ~6000 μg/m^3 by FALL3D + WRF_ERA. Therefore, FALL3D + WRF_ERA generated concentrations that exceed the value described by FALL3D + WRF_GFS by more than 50%. As shown in Table 1 in Raga et al. (2013), flights operations at Jorge Newbery and Ezeiza airports were not cancelled on June 8, 2011. Since the Buenos Aires VAAC has no records of admissible ash concentration limits for flights, London's VAAC standard may be considered instead (Witham et al., 2012). According to this classification, the results of the FALL3D + WRF_GFS system corresponded to a medium contamination area while FALL3D + WRF_ERA, to a high contamination area. Considering a null hypothesis with mean ash concentrations found at site over 4000 μg/m^3 and an alternative hypothesis with a level below 4000 μg/m^3, and considering that flights scheduled were not cancelled (which would imply concentrations < 4000 μg/m^3) on June 8, 2011, the FALL3D + WRF_GFS diagnosis generated an output that is more consistent with what happened (alternative hypothesis). In this context, with the FALL3D + WRF_ERA system as reference, a Type II error would have been generated, which would have concluded that ash concentrations at heights did not comply with London's VAAC standards and, therefore, those flights would have been canceled. This situation highlights the importance of evaluating meteorological uncertainties using the volcanic ash modeling system. Moreover, the eventual adoption by ICAO of other quantitative safety thresholds of ash concentration would also have important implications for modeling strategies.

5. Conclusions

In this study, we evaluated the effects of the ERA-Interim reanalysis and the NCEP-GFS analysis used as dynamic conditions of the WRF model, on the dispersion of volcanic ash calculated by FALL3D, as well as the propagation of the meteorological errors in the transport model in the SVZ region. The case used for analysis was the eruption of PCCVC, which took place during a 10-day period on June 2011.

It was proposed that the FALL3D + WRF system is sensitive to changes in dynamic conditions (NCEP-GFS and ERA-Interim) and, therefore, such conditions might affect the simulation of the volcanic ash dispersion. In this work, we hypothesized that the greatest uncertainty in the meteorological variables that are transferred to the ash dispersion model would be in the horizontal wind direction.

In the first stage of this work, the methodology applied allowed us to evaluate, for the radio sounding stations set, the performance of the WRF model combined with NCEP-GFS and ERA-Interim in relation to the representation of different error types (RMSE, RMSD, MBE, MBE + σbias, and DISP). The study showed that the performance of WRF_GFS and WRF_ERA errors depend on height. In this context, the statistical analysis revealed that, in general, for the variables analyzed, WRF_GFS had a better performance mainly between 925 and 300 hPa.

In the second stage of this work, due to the differences between the ash mass load of FALL3D + WRF_GFS and FALL3D + WRF_ERA evidenced by MODIS, the dominant meteorological conditions of WRF_GFS and WRF_ERA were analyzed from a synoptic and a dynamic

perspective. The main goal was to determine which physical processes contributed to establishing differences in the net transport of the volcanic plume between the two configurations. At first, we observed that the differences in the ash mass load between FALL3D + WRF_GFS and FALL3D + WRF_ERA were a result of the existing differences in horizontal wind direction between WRF_GFS and WRF_ERA. However, we found that those differences in horizontal wind direction and intensity are the consequence of differences in the horizontal gradients of the geopotential heights between the two meteorological simulations at the different atmospheric levels. Therefore, it should be noted that the geopotential height fields generated by WRF_GFS show more intense high and low pressure systems, which in turn cause the higher intensity of the winds in study area. In addition, WRF_GFS generates a layer mean temperature lower (colder) than that given by WRF_ERA.

The main conclusion of this study emphasizes that it is not the same to use any dynamic condition in the meteorological model in order to simulate volcanic ash dispersion in the SVZ region. According to Roberts and Knippertz (2014), it is noteworthy that the largest impact on WRF simulation outputs come from varying the initial and boundary conditions (i.e. NCEP-GFS analysis or ERA-interim reanalysis) rather than changes within the WRF model physics itself. The difference between varying these global products is given by differences between the 6-hourly 3D-VAR and the 12-hourly 4D-VAR data assimilation systems employed by NCEP-GFS and ERA-Interim, respectively. These assimilation systems can be affected by 1) observational data availability to be assimilated and 2) observational data density assimilated for them. With respect to the first point, as shown in Section 2.2.3 and Table 2, observational data availability to be assimilated can differ for analysis and reanalysis because for example in situ upper-air measurements may not always be regularly available. Additionally, 4D-VAR is more sensitive to data availability since it fills in gaps in output variables, especially in data-sparse regions, and constrains variables to be more physically consistent (Smith et al., 2014). Regarding the second aspect, 4D-VAR uses observational data at their actual time of measurements and all temporally continuous observational data available within a 12-hour analysis window, with its corresponding varying error covariances in time. While 3D-VAR treats observational valid data at 00, 06, 12, or 18 UTC, it uses temporally continuous observational data only close to synoptic times (6-hour analysis window) with static error covariances. In consequence, the temporal averaging or smoothing intrinsic in 4D-VAR may affect WRF_ERA results (see for example, Rood and Bosilovich, 2010; Smith et al., 2014).

The second conclusion of the study is that, at regional scales, special attention should be given not only to the propagation of errors caused by wind direction and intensity but also to errors derived from the geopotential heights, since these will have an impact on the net transport of horizontal and vertical dispersion of volcanic ash caused by turbulence as well as on volcanic plume transport speed.

The third conclusion of this work is that NCEP-GFS would seem to be the best option to use as initial and lateral boundary condition of the WRF model in the SVZ region. In this way, the system that results from the combination of the WRF model initialized with NCEP-GFS and the FALL3D dispersion model would provide reasonably accurate results in order to estimate the position of the ash plume and deposit in the SVZ region.

This study lays a good foundation for the development of an ash dispersion modeling system based on a prior evaluation of meteorological errors.

Acknowledgments

Authors acknowledge the NCEP for the GFS analysis dataset and the ECMWF for the ERA-Interim reanalysis dataset, with documentation available on http://www.emc.ncep.noaa.gov/index.php?branch=GFS and http://www.ecmwf.int/en/research/climate-reanalysis/era-interim, respectively. Authors also gratefully acknowledge the ESA for providing GlobCover 2009 (© ESA 2010 & UC Louvain), the MODIS Science Data Support Team (http://modis.gsfc.nasa.gov/) and the NASA's Earth Observing System Data and Information System (http://reverb.echo.nasa.gov/reverb/) for processing and distributing MODIS data used in this article, respectively. The authors gratefully acknowledge the assistance of the editor-in-chief of Atmospheric Research, Ph D. Jose Luis Sánchez, in editing the manuscript and the anonymous reviewer for his/her detailed and helpful comments to the manuscript. This work was supported by Consejo Nacional de Investigaciones Científicas y Técnicas (CONICET), Universidad Tecnológica Nacional (UTN) of Argentina, under grant project no. PID UTN IFI1487 Cod. 25/JC01 and PICT 2012-1021.

Appendix A. Comparison between NCEP-GFS and ERA-Interim datasets in the southern cone of South America

Widespread used reanalysis include the National Center for Environmental Prediction/Global Forecast System (NCEP-GFS hereafter) and the European Centre for Medium-Range Weather Forecasts (ECMWF) ERA-Interim, covering the data since 2004 and 1979, respectively. Since these datasets present different spatial resolution and are initialized with a wide variety of weather observations, including satellite measurements, it is expected that meteorological continuous simulations, with one single initialization of large-scale fields and frequent updates of boundary conditions from different dynamic conditions, produce dissimilar outputs. Furthermore, NCEP-GFS is assimilated using a 6-hourly Three-Dimensional Variational Assimilation Data system (3D-VAR), but ERA-Interim is based on a 12-hourly Four-Dimensional Variational Assimilation Data system (4D-VAR).

To illustrate the differences between both reanalysis and analysis, we present Fig. A1, which shows, as example, the spatial difference between air temperature patterns in the Southern Volcanic Zone (SVZ) region for different standard pressure levels at June 06, 2011, at 12:00 UTC. The data used for this comparison have been gridded onto a 0.5° and 0.75° longitude–latitude grid for NCEP-GFS and ERA-Interim, respectively. From this figure, slight differences in air temperature over water (between 75°W and 80°W) at all pressure levels can be noticed. The basic features present in NCEP-GFS are very similar to those observed in ERA-Interim. Most notable is the contrasting warm and cold regions over land, particularly at latitudes lower to 40°S.

The main differences between NCEP-GFS and ERA-Interim at 850 hPa seem to occur preferably over the continent. Both patterns agree well to represent the latitudinal temperature gradient, although minor local differences in their magnitude are also apparent. Examining Fig. A1, it is evident that the ERA-Interim and the NCEP-GFS values have compared better at the 500 hPa, although NCEP-GFS air temperatures are slightly higher at low latitudes over land. The most significant discrepancy between analysis and reanalysis occurs at high levels (i.e., 300 hPa) with differences up to 5 °C. It is also interesting to note that the minimum values of air temperature at 300 hPa are located over land on the center part of the continent in NCEP-GFS, but for ERA-Interim, they extend over the Atlantic Ocean. In Fig. A1, local minima and maxima are seen over the same regions, but with different values.

It is worth also mentioning that significant differences due to the available observations between both global data at these regions cannot be excluded because it is unclear how many real measurements (e.g., radiosonde data) went into the reanalysis/analysis at these locations.

Appendix B. Statistical analysis summary

Model agreement to measurements was evaluated using several performance statistics: root mean square error or total error (RMSE),

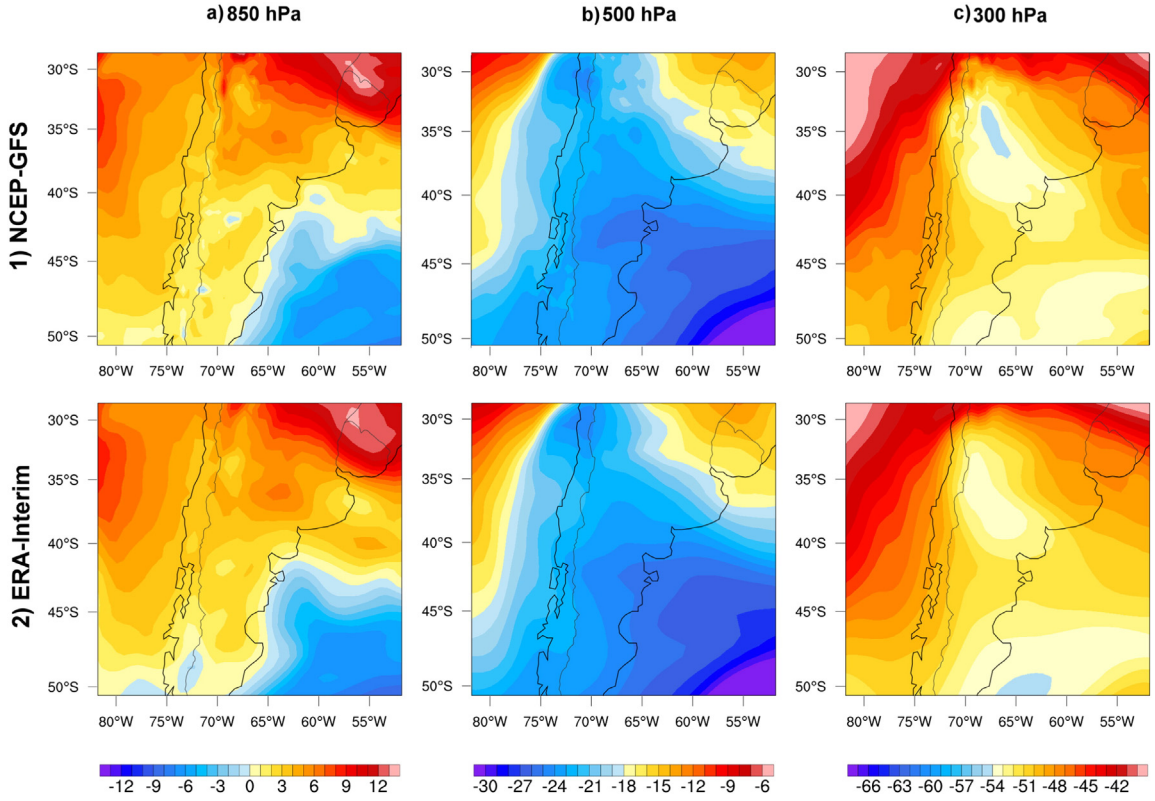

Fig. A1. Air-temperature (°C) for NCEP-GFS and ERA-Interim in the SVZ region at three standard pressure levels (850, 500, and 300 hPa) (date: June 06, 2011, at 12:00 UTC).

mean bias error (MBE), unbiased root mean square difference (RMSD), variability error (σbias), dispersion or phase error (DISP), and amplitude error (MBE + σbias).

Given θ^{sim} and θ^{obs} which represent simulated and observed time series of a meteorological variable, respectively, the error can be defined as the difference between the variable simulated value (θ_i^{sim}) and the variable observed value (θ_i^{obs}), for each time interval i (1). The time interval i range from 0 to *k*, where *k* is the total number of pairs of simulation/observed records.

The total error (RMSE) is the square root of the mean/average of the square of all of the error which is called mean square error (MSE) (2).

RMSE can be broken down into two components (2), as shown in several studies (Takacs, 1985; Hou et al., 2001; Lange, 2005), one related to the bias error (MBE) and another, the unbiased error (RMSD). Bias can be defined by means of MBE and it is calculated (3) as the difference or bias between simulated and observed mean values, $\overline{\theta^{sim}}$ and $\overline{\theta^{obs}}$, respectively, which allows data tendency to be evaluated. A positive bias indicates that simulations overestimate the observed values and a negative bias indicates the opposite.

RMSD (4) is a measure of the error variability around its mean. RMSD is made up of different terms. The first of these is σbias (5), which quantifies the errors due to the simulation's lack of accuracy through simulated and observed standard deviations, σ^{sim} and σ^{obs}, respectively. The DISP error (6) contributes the phase errors to RMSE, and it is estimated through σ^{sim}, σ^{obs} , and the cross-correlation coefficient between θ^{sim} and θ^{obs} (R). Additionally, σbias is related to amplitude error like MBE (7). It should be noted that phase errors are statistically interpreted in terms of cross-correlations and not as phase changes in two time series. Phase errors constitute a serious setback to the model's performance. Amplitude errors, on the other hand, can be resolved by means of linear correlations.

Table A1
Typical errors used to evaluate the model's performance.

Errors	Expressions	Ref. in text
Error	$\theta_i = \theta_i^{sim} - \theta_i^{obs} \quad i = 0..k$	(1)
RMSE	$RMSE = \sqrt[2]{MSE}$ where $MSE = \frac{1}{k}\sum_{i=0}^{k}\theta_i^2$ $RMSE = \sqrt{MBE^2 + RMSD^2}$	(2)
MBE	$MBE = \frac{1}{k}\sum_{i=0}^{k}\theta_i = \overline{\theta^{sim}} - \overline{\theta^{obs}}$ where $\overline{\theta^{sim}} = \frac{1}{k}\sum_{i=0}^{k}\theta_i^{sim}$ and $\overline{\theta^{obs}} = \frac{1}{k}\sum_{i=0}^{k}\theta_i^{obs}$	(3)
RMSD	$RMSD = \sqrt{RMSE^2 - MBE^2}$ and $RMSD^2 = \sigma bias^2 + DISP^2$ then $RMSE = \sqrt{MBE^2 + \sigma bias^2 + DISP^2}$	(4)
σbias	$\sigma bias = \sigma^{sim} - \sigma^{obs}$	(5)
DISP	$DISP = \sqrt{2\sigma^{sim}\sigma^{obs}(1-R)}$	(6)
Amplitude error	MBE + σbias	(7)

References

Adame, J.A., Valentí-Pía, M.D., Gil-Ojeda, M., 2015. Impact evaluation of potential volcanic plumes over Spain. Atmos. Res. 160, 39–49.
Andronache, C., 2004. Estimates of sulfate aerosol wet scavenging coefficient for locations in the Eastern United States. Atmos. Environ. 38, 795–804.
Berens, P., 2009. CircStat: a MATLAB toolbox for circular statistics. J. Stat. Softw. 31, 1–21.

Bonasia, R., Costa, A., Folch, A., Macedonio, G., Capra, L., 2012. Numerical simulation of tephra transport and deposition of the 1982 El Chichón eruption and implications for hazard assessment. J. Volcanol. Geotherm. Res. 231-232, 39–49.

Borge, R., Alexandrov, V., Josedelvas, J., Lumbreras, J., Rodriguez, E., 2008. A comprehensive sensitivity analysis of the WRF model for air quality applications over the Iberian Peninsula. Atmos. Environ. 42, 8560–8574.

Brioude, J., Angevine, W., McKeen, S., Hsie, E., 2012. Numerical uncertainty at mesoscale in a Lagrangian model in complex terrain. Geosci. Model Dev. Discuss. 5, 967–991.

Bulletin of the Global Volcanism Network (BGVN), 2012. http://www.volcano.si.edu/world/volcano.cfm?vnum=1507-15=&volpage=var (accessed 02/20/2012).

Bursik, M., 2001. Effect of wind on the rise height of volcanic plumes. Geophys. Res. Lett. 28, 3621–3624.

Byun, D., Schere, K.L., 2006. Review of the governing equations, computational algorithms, and other components of the Models-3 Community Multiscale Air Quality (CMAQ) Modeling System. Appl. Mech. Rev. 59, 51–77.

Carazzo, G., Kaminski, E., Tait, S., 2006. The route to self-similarity in turbulent jets and plumes. J. Fluid Mech. 547, 137–148.

Carn, S., Krueger, A., Krotkov, N., Yang, K., Evans, K., 2009. Tracking volcanic sulfur dioxide clouds for aviation hazard mitigation. Nat. Hazards 51, 325–343.

Carvalho, D., Rocha, A., Gómez-Gesteira, M., 2012. Ocean surface wind simulation forced by different reanalyses: comparison with observed data along the Iberian Peninsula coast. Ocean Model. 56, 31–42.

Carvalho, D., Rocha, A., Gómez-Gesteira, M., Silva Santos, C., 2014. WRF wind simulation and wind energy production estimates forced by different reanalyses: comparison with observed data for Portugal. Appl. Energy 117, 116–126.

Casadevall, T.J., 1994. The 1989–1990 eruption of Redoubt Volcano, Alaska: impacts on aircraft operations. J. Volcanol. Geotherm. Res. 62, 301–316.

Casadevall, T.J., Krohn, M.D., 1995. Effects of the 1992 Crater Peak eruption on airports and aviation operations in the United States and Canada. U.S. Geol. Surv. Bull. 2139, 205–220.

Costa, A., Macedonio, G., Folch, A., 2006. A three-dimensional Eulerian model for transport and deposition of volcanic ashes. Earth Planet. Sci. Lett. 241, 634–647.

Cullen, M.J.P., 1993. The unified forecast/climate model. Meteorol. Mag. 122, 81–94.

Dee, D.P., Uppala, S.M., Simmons, A.J., Berrisford, P., Poli, P., Kobayashi, S., Andrae, U., Balmaseda, M.A., Balsamo, G., Bauer, P., Bechtold, P., Beljaars, A.C.M., van de Berg, L., Bidlot, J., Bormann, N., Delsol, C., Dragani, R., Fuentes, M., Geer, A.J., Haimberger, L., Healy, S.B., Hersbach, H., Hólm, E.V., Isaksen, L., Kållberg, P., Köhler, M., Matricardi, M., McNally, A.P., Monge-Sanz, B.M., Morcrette, J.-J., Park, B.-K., Peubey, C., de Rosnay, P., Tavolato, C., Thépaut, J.-N., Vitart, F., 2011. The ERA-Interim reanalysis: configuration and performance of the data assimilation system. Q. J. R. Meteorol. Soc. 137, 553–597.

Dudhia, J., 1989. Numerical study of convection observed during the winter monsoon experiment using a mesoscale two-dimensional model. J. Atmos. Sci. 46, 3077–3107.

Ek, M.B., Mitchell, K.E., Lin, Y., Rogers, E., Grunmann, P., Koren, V., Gayno, G., Tarpley, J.D., 2003. Implementation of Noah land surface model advances in the National Centers for Environmental Prediction operational mesoscale Eta model. J. Geophys. Res. Atmos. 108, 8851.

Folch, A., Costa, A., Macedonio, G., 2009. FALL3D: a computational model for transport and deposition of volcanic ash. Comput. Geosci. 35, 1334–1342.

Folch, A., Costa, A., Basart, S., 2012. Validation of the FALL3D ash dispersion model using observations of the 2010 Eyjafjallajökull volcanic ash clouds. Atmos. Environ. 48, 165–183.

Ganser, G., 1993. A rational approach to drag prediction of spherical and nonspherical particles. Powder Technol. 77, 143–152.

Gislason, S.R., Hassenkam, T., Nedel, S., Bovet, N., Eiriksdottir, E.S., Alfredsson, H.A., Hem, C.P., Balogh, Z.I., Dideriksen, K., Oskarsson, N., Sigfusson, B., Larsen, G., Stipp, S.L.S., 2011. Characterization of Eyjafjallajokull volcanic ash particles and a protocol for rapid risk assessment. Proc. Natl. Acad. Sci. U. S. A. 108, 7307–7312.

Guenther, B., Godden, G.D., Xiong, X., Knight, E.J.S.-Y.Q., Montgomery, H., Hopkins, M.M., Khayat, M.G., Hao, Z., 1998. Prelaunch algorithm and data format for the Level 1 calibration products for the EOS-AM1 Moderate Resolution Imaging Spectroradiometer (MODIS). IEEE Trans. Geosci. Remote Sens. 36, 1142–1151.

Guffanti, M., Mayberry, G.C., Casadevall, T.J., Wunderman, R., 2008. Volcanic hazards to airports. Nat. Hazards 51, 287–302.

Guffanti, B.M., Casadevall, T.J., Budding, K., 2010. Encounters of aircraft with volcanic ash clouds: a compilation of known incidents, 1953–2009: U.S. Geological Survey Data Series 545, ver. 1.0, 12, plus 4 appendixes including the compilation database. http://pubs.usgs.gov/ds/545/ (accessed 08/20/2015).

Hanna, S.R., Strimaitis, D.G., 1990. Rugged terrain effects on diffusion. Atmos. Process. over complex terrain. Meteorol. Monogr. 23, 109–143.

Hong, S.Y., 2010. A new stable boundary-layer mixing scheme and its impact on the simulated East Asian summer monsoon. Q. J. R. Meteorol. Soc. 136, 1481–1496.

Hong, S.Y., Dudhia, J., Chen, S.H., 2004. A revised approach to ice microphysical processes for the bulk parameterization of clouds and precipitation. Mon. Weather Rev. 132, 103–120.

Hou, D., Kalnay, E., Droegemeier, K.K., 2001. Objective verification of the SAMEX'98 ensemble forecasts. Mon. Weather Rev. 129, 73–91.

Kain, J.S., 2004. The Kain–Fritsch convective parameterization: an update. J. Appl. Meteorol. 43, 170–181.

Katurji, M., Zhong, S., Zawar-Reza, P., 2011. Long-range transport of terrain-induced turbulence from high-resolution numerical simulations. Atmos. Chem. Phys. 11, 11793–11805.

King, M.D., Kaufman, Y.J., Menzel, W.P., Tanre, D., 1992. Remote sensing of cloud, aerosol, and water vapor properties from the moderate resolution imaging spectrometer (MODIS). IEEE Trans. Geosci. Remote Sens. 30, 2–27.

Kuo, C.-C., Gan, T.Y., Hanrahan, J.L., 2014. Precipitation frequency analysis based on regional climate simulations in Central Alberta. J. Hydrol. 510, 436–446.

Kvietkus, K., Šakalys, J., Didžbalis, J., Garbariene, I., Špirkauskaite, N., Remeikis, V., 2013. Atmospheric aerosol episodes over Lithuania after the May 2011 volcano eruption at Grimsvötn, Iceland. Atmos. Res. 122, 93–101.

Lange, M., 2005. On the uncertainty of wind power predictions—analysis of the forecast accuracy and statistical distribution of errors. J. Sol. Energy Eng. 127, 177–184.

Laprise, R., 1992. The Euler equations of motion with hydrostatic pressure as an independent variable. Mon. Weather Rev. 120, 197–207.

Lara, L.E., Moreno, H., Naranjo, J.A., Matthews, S., Pérez de Arce, C., 2006. Magmatic evolution of the Puyehue–Cordón Caulle Volcanic Complex (40°S), Southern Andean Volcanic Zone: from shield to unusual rhyolitic fissure volcanism. J. Volcanol. Geotherm. Res. 157, 343–366.

Macedonio, G., Costa, A., Longo, A., 2005. A computer model for volcanic ash fallout and assessment of subsequent hazard. Comput. Geosci. 31, 837–845.

Mann, H.B., Whitney, D.R., 1947. On a test of whether one of two random variables is stochastically larger than the other. Ann. Math. Stat. 18, 50–60.

Merzlyakov, E.G., Solovjova, T.V., Yudakov, A.A., 2013. The interannual variability of a 5-7 day wave in the middle atmosphere in autumn from ERA product data, Aura MLS data, and meteor wind data. J. Atmos. Sol. Terr. Phys. 102, 281–289.

Michalakes, J., Dudhia, J., Gill, D., Henderson, T., Klemp, J., Skamarock, W., Wang, W., 2004. The Weather Research and Forecast Model: Software Architecture and Performance to appear in proceedings of the 11th ECMWF Workshop on the Use of High Performance Computing In Meteorology, 25–29 October 2004.

Miller, T.P., Casadevall, T.J., 2000. Volcanic ash hazards to aviation. In: Sigurdsson, H. (Ed.), Encyclopedia of Volcanoes. Academic Press, San Diego, pp. 915–930.

Mlawer, E.J., Taubman, S.J., Brown, P.D., Iacono, M.J., Clough, S.A., 1997. Radiative transfer for inhomogeneous atmospheres: RRTM, a validated correlated-k model for the longwave. J. Geophys. Res. Atmos. 102, 16663–16682.

MM5 Community Model Homepage, http://www2.mmm.ucar.edu/mm5/n.d. (accessed 08/29/2015).

Prata, A.J., 1989. Observations of volcanic ash clouds in the 10–12 μm window using AVHRR/2 data. Int. J. Remote Sens. 10, 751–761.

Prata, F., Bluth, G., Rose, B., Schneider, D., Tupper, A., 2001. Comments on "Failures in detecting volcanic ash from a satellite-based technique". Remote Sens. Environ. 78, 341–346.

Puliafito, S.E., Allende, D.G., Mulena, G.C., Cremades, P., Lakkis, S.G., 2015. Evaluation of the WRF model configuration for Zonda wind events in a complex terrain. Atmos. Res. 166, 24–32.

Raga, G.B., Baumgardner, D., Ulke, A.G., Torres Brizuela, M., Kucienska, B., 2013. The environmental impact of the Puyehue–Cordon Caulle 2011 volcanic eruption on Buenos Aires. Nat. Hazards Earth Syst. Sci. 13, 2319–2330.

Roberts, A.J., Knippertz, P., 2014. The formation of a large summertime Saharan dust plume: convective and synoptic-scale analysis. J. Geophys. Res. Atmos. 119, 1766–1785.

Rodriguez, E., Morris, C.S., Belz, J.E., Chapin, E.C., Martin, J.M., Daffer, W., Hensley, S., 2005. An assessment of the SRTM topographic products. Technical Report JPL D-31639, Jet Propulsion Laboratory. Pasadena, California, p. 143.

Rojas-Ramos, M., Catalan-Vazquez, M., Martin-Del Pozzo, A.L., Garcia-Ojeda, E., Villalba-Caloca, J., Perez-Neria, J., 2001. A seven months prospective study of the respiratory effects of exposure to ash from Popocatepetl Volcano, Mexico. Environ. Geochem. Health 23, 379–392.

Rood, R.B., Bosilovich, M.G., 2010. Reanalysis: data assimilation for scientific investigation of climate. In: Lahoz, W., Khattatov, B., Menard, R. (Eds.), Data Assimilation: Making Sense of Observations. Springer Berlin Heidelberg, Berlin, Heidelberg, pp. 623–646.

Rose, W.I., Mayberry, G.C., 2000. Use of GOES thermal infrared imagery for eruption scale measurements, Soufrière Hills, Montserrat. Geophys. Res. Lett. 27, 3097–3100.

Ryall, D.B., Maryon, R.H., 1998. Validation of the UK Met. Office's NAME model against the ETEX dataset. Atmos. Environ. 32, 4265–4276.

Satyamurty, P., Nobre, C., Silva Dias, P., 1998. South America. In: Karoly, D., Vincent, D. (Eds.), Meteorology of the Southern Hemisphere. American Meteorological Society, Boston, USA, pp. 119–139.

Scaini, C., Folch, A., Navarro, M., 2012. Tephra hazard assessment at Concepción Volcano, Nicaragua. J. Volcanol. Geotherm. Res. 219-220, 41–51.

Scollo, S., Folch, A., Costa, A., 2008. A parametric and comparative study of different tephra fallout models. J. Volcanol. Geotherm. Res. 176, 199–211.

Scollo, S., Prestifilippo, M., Spata, G., D'Agostino, M., Coltelli, M., 2009. Monitoring and forecasting Etna volcanic plumes. Nat. Hazards Earth Syst. Sci. 9, 1573–1585.

Scott, B.C., Luecken, D.J., 1992. The sensitivity of modeled sulfate wet deposition to the meteorological values used as input. Atmos. Environ. Part A 26, 559–569.

SERNAGEOMIN, 2011. Southern Andes Volcanological Observatory-National Geology, Mining Service Homepage. http://www.sernageomin.cl/volcan-observatorio.php (accessed 07/07/2011).

Sertel, E., Robock, A., Ormeci, C., 2010. Impacts of land cover data quality on regional climate simulations. Int. J. Climatol. 30, 1942–1953.

Shibata, T., Kinoshita, T., 2016. Volcanic aerosol layer formed in the tropical upper troposphere by the eruption of Mt. Merapi, Java, in November 2010 observed by the spaceborne lidar CALIOP. Atmos. Res. 168, 49–56.

Siebert, L., Simkin, T., 2002. Volcanoes of the world: an illustrated catalog of Holocene Volcanoes and their eruptions. Smithsonian Institution, Global Volcanism Program Digital Information Series, GVP-3. http://www.volcano.si.edu (accessed 06/08/2015).

Siebert, L., Simkin, T., Kimberly, P., 2010. Volcanoes of the World. third ed. University of California Press, Berkeley, p. 568.

Simpson, J.J., Berg, J.S., Hufford, G.L., Bauer, C., Pieri, D., Servranckx, R., 2002. The February 2001 eruption of Mount Cleveland, Alaska: case study of an aviation hazard. Weather Forecast. 17, 691–704.

Skamarock, W.C., Klemp, J.B., Gill, D.O., Barker, D.M., Wang, W., Powers, J.G., 2008. A description of the advanced research WRF Version 3. Mesoscale microscale meteorol. Div. Natl. Cent. Atmos. Res.

Smith, C.A., Compo, G.P., Hooper, D.K., 2014. Web-Based Reanalysis Intercomparison Tools (WRIT) for analysis and comparison of reanalyses and other datasets. Bull. Am. Meteorol. Soc. 95, 1671–1678.

Spence, R.J.S., Kelman, I., Baxter, P.J., Zuccaro, G., Petrazzuoli, S., 2005a. Residential building and occupant vulnerability to tephra fall. Nat. Hazards Earth Syst. Sci. 5, 477–494.

Spence, R.J.S., Kelman, I., Calogero, E., Toyos, G., Baxter, P.J., Komorowski, J.-C., 2005b. Modelling expected physical impacts and human casualties from explosive volcanic eruptions. Nat. Hazards Earth Syst. Sci. 5, 1003–1015.

Spiridonov, V., Ćurić, M., 2012. Examination of sulfate chemistry sensitivity in a mid-latitude and tropical storm using a cloud resolving model. Asia-Pac. J. Atmos. Sci. 48, 391–410.

Sulpizio, R., Mele, D., Dellino, P., Volpe, L., 2005. A complex, Subplinian-type eruption from low-viscosity, phonolitic to tephri-phonolitic magma: the AD 472 (Pollena) eruption of Somma-Vesuvius, Italy. Bull. Volcanol. 67, 743–767.

Takacs, L.L., 1985. A two-step scheme for the advection equation with minimized dissipation and dispersion errors. Mon. Weather Rev. 113, 1050–1065.

Thomas, H.E., Prata, A.J., 2011. Sulphur dioxide as a volcanic ash proxy during the April–May 2010 eruption of Eyjafjallajökull Volcano, Iceland. Atmos. Chem. Phys. 11, 6871–6880.

Tsunematsu, N., Nagai, T., Murayama, T., Adachi, A., Murayama, Y., 2008. Volcanic ash transport from Mount Asama to the Tokyo metropolitan area influenced by large-scale local wind circulation. J. Appl. Meteorol. Climatol. 47, 1248–1265.

Unidata/University Corporation for Atmospheric Research (UCAR), National Centers for Environmental Prediction/National Weather Service/NOAA/U.S. Department of Commerce, and European Centre for Medium-Range Weather Forecasts, 2003. Historical Unidata Internet Data Distribution (IDD) Gridded Model Data. Research Data Archive at the National Center for Atmospheric Research, Computational and Information Systems Laboratory. http://rda.ucar.edu/datasets/ds335.0/ (accessed 08/08/2011).

Wilson, T., Cole, J., Stewart, C., Cronin, S., Johnston, D., 2011. Ash storms: impacts of wind-remobilised volcanic ash on rural communities and agriculture following the 1991 Hudson eruption, southern Patagonia, Chile. Bull. Volcanol. 73, 223–239.

Witham, C., Webster, H., Hort, M., Jones, A., Thomson, D., 2012. Modelling concentrations of volcanic ash encountered by aircraft in past eruptions. Atmos. Environ. 48, 219–229.

Woodhouse, M.J., Hogg, A.J., Phillips, J.C., Sparks, R.S.J., 2013. Interaction between volcanic plumes and wind during the 2010 Eyjafjallajökull eruption, Iceland. J. Geophys. Res. Solid Earth 118, 92–109.

Yu, T.X., Rose, W.I., Prata, A.J., 2002. Atmospheric correction for satellite-based volcanic ash mapping and retrievals using “split window” IR data from GOES and AVHRR. J. Geophys. Res. Atmos. 107, 4311.